Optimization of Interdigitated Sensor Characteristics

J. Claudel, A. L. Alves de Araujo, D. Kourtiche, M. Nadi, and A. Bourjilat

Abstract Interdigitated sensors for bioimpedance analysis (BIA) are specially adapted for the characterization of low-volume (microliter scale) biological samples and the monitoring of a thin-film of biological cells for cell culture or cell settling and coagulation analysis. Impedance spectroscopy has the advantage of being a marker-free method (a combined impedance and marker is also possible), which considerably simplifies the preparation of samples. The geometry of the interdigitated sensor simultaneously represents microscopic sizes as the electrodes' width, gap, and millimetric surface, making the sample deposition easier. The microscopic size of the electrodes induces an increase in double-layer effects, which can completely occult interesting bandwidth of the impedance measurements. This effect, therefore, must be considered early in the sensor optimization design. In this work, we propose a complete approach to optimize interdigitated sensors according to targeted applications. A complete analytical model is proposed and validated with a finite element method simulation using COMSOL Multiphysics software. The model examines the influence of all geometrical parameters, such as number of electrodes, width, gap, and substrate material. A detailed methodology is proposed to choose the best compromise between sensitivity and useful bandwidth. To validate the proposed methodology, measurements were performed on biological samples (yeast cells) using five sensors with different optimized geometries. Results demonstrated the validity of the proposed methodology and the possibility to extract all the intrinsic electrical parameters of the biological samples using both optimized sensors and our models.

J. Claudel · A. L. Alves de Araujo · D. Kourtiche · M. Nadi (✉) · A. Bourjilat
Institut Jean Lamour, Lorraine University (CNRS—UMR 7198), 54011 Nancy, France
e-mail: mustapha.nadi@univ-lorraine.fr

J. Claudel
e-mail: julien.claudel@univ-lorraine.fr

1   Introduction

Since the invention of Clark's electrode oxygen sensor (1956) [1], many improvements in the sensitivity, selectivity, and multiplexing of biosensors (Lab-on-chip) have emerged. Biosensors can be defined as a compact analytical device incorporating a biological detection element associated with a physicochemical transducer [2]. These methods are often based on charge transfer sensors, impedance-based sensors, and capacitance-based sensors. Impedance spectroscopy is now well known as a powerful technique for biological sensing characterization at both macroscopic and microscopic scales [3]. Electrodes serve for applying an electric field to the sample under test and for measuring the electrical detection signals. They also can provide information on relative permittivity and electrical conductivity of the biosamples, which correspond to intrinsic parameters [4]. At the macroscopic scale, impedance sensors are generally composed of two parallel plates where the sample is enclosed. They are easy to use but need a large quantity of biosamples (few to tens of mL). Moreover, electrodes only provide average information about the whole sample. On the contrary, the combination of impedance spectroscopy and microscopic electrodes, such as interdigitated sensors [5], provides more sensitive sensors that can analyze, at the microscopic scale, cell surface cultures [6], cell settling, and trapped bacteria, as well as detecting DNA oligonucleotides [7]. Beyond a simple interface, the geometrical properties of electrodes can have a significant impact on the efficiency of the biosensor [8, 9]. They need to be optimized a priori during the sensors' design step according to the targeted application and the nature of the cells to analyze [10, 11]. To achieve this optimization of the sensor design, we present a detailed methodology to define the best interdigitated structure according to the targeted application.

In the first section, a complete and detailed analytical model is presented. The model considers all the sensor's parameters, such as the electrode length, gap, width, and electrical properties of the medium. Moreover, it accounts for double-layer effects. The model is based on the impedance model of a pair of electrodes, extended to a succession of electrodes, and considering edge effects. The model was validated using simulation by the finite element method (FEM).

In the following section, "Interdigitated sensor optimization," the effects of all geometrical parameters were tested independently to determine their impact on bioimpedance measurements. One important purpose is to maintain a sufficiently wide bandwidth to characterize the biosample over many decades. To obtain the correct optimization, which consists of the best compromise between bandwidth and sensitivity, a detailed optimization methodology is presented. A step-by-step description appears at the end of this section.

The last section focuses on the experimental validation of the two previous sections. Five sensor designs with different degrees of optimization were fabricated using a classical microfabrication process. Characterizations were performed on calibrated electrolytic solutions and yeast cells samples by a conventional macroscopic probe and compared to the measurement performed with fabricated sensors.

2 Analytical Method

2.1 Coplanar Electrodes

Interdigitated electrodes are based on a succession of coplanar microelectrodes. The first step is to model the electrical response, which depends on the electric field distribution between a pair of coplanar electrodes. This pair of electrodes is assumed to be an electric capacitor. For standard parallel capacitors, electrodes are placed face-to-face with a uniform distribution of the electric field. When electrodes are gradually opened, the electric field extends in a wider space and generates a fringing field. However, if the electrodes open on a planar plane, the fringing field becomes heterogeneously allocated between the electrodes, and one obtains a coplanar electrode sensor [12]. Figure 1 illustrates the evolution from a parallel plate capacitor to a coplanar electrodes' sensor.

A simplified analysis for calculating the capacity of a pair of semi-infinite electrodes is first used to introduce two important design quantities, namely the penetration depth of the field T and the effective width of electrodes W_{eff}. The two-dimensional distribution of the electric field for this geometry can easily be solved with conformal mapping techniques using an inverse cosine transform [13]. For semi-finished electrodes, the capacity of a pair of finite-width electrodes w and gap g can be calculated as follows:

$$C = \frac{Q}{2V_0} = \frac{2\varepsilon_0 \varepsilon_r L}{\pi} \ln \left[\sqrt{\left(1 + \frac{w}{a}\right)^2 - 1} + \left(1 + \frac{w}{a}\right) \right] \tag{1}$$

where Q is the total charge of a single electrode, ε_0 the permittivity of the vacuum, L is the length of the electrodes and $a = g/2$. For $L \gg w$, Eq. (1) provides a reliable estimation of the capacity for a pair of coplanar electrodes with finite width ($w/g \gg 1$). The electrode's width w establishes a maximum field penetration depth T in a medium whose thickness is labeled by h_{med}. The penetration depth is calculated from the elliptic contours, which correspond to the intensity of the field at a fixed position $r = (x^2 + y^2)^{-1/2}$. T corresponds to the vertical displacement of the electric
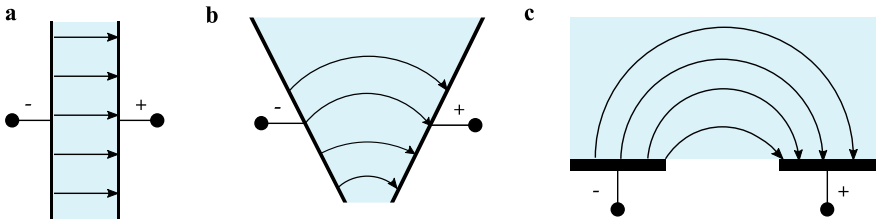

Fig. 1 Transition of a parallel to a coplanar electrode capacitor. **a** Parallel electrode sensor, **b** open transition, and **c** coplanar electrode capacitor

field line issued from the end of the electrode and can be calculated as follows:

$$T = a \sinh\left[\cosh^{-1}\left(1 + \frac{w}{a}\right)\right] = a\sqrt{\left(1 + \frac{w}{a}\right)^2 - 1} \qquad (2)$$

For a medium whose thickness $\mathbf{h_{med}} < \mathbf{T}$, the capacitance is determined only by the electric field lines emanating from the effective width $\mathbf{W_{eff}}$, as shown in Eq. (3).

$$\frac{w_{eff}}{a} = a\sqrt{\left(1 + \frac{h_{med}}{a}\right)^2 - 1} \qquad (3)$$

This concept of effective width is only applicable when the permittivity of the dielectric environment is higher than that of the air. This is the case for water-based solutions. The ratio $\mathbf{h_{med}}/\mathbf{T}$ can be used as an approximate indicator of the signal detection level for this electrode geometry. When $\mathbf{h_{med}} \gg \mathbf{T}$, the capacity does not depend on the sample thickness. This is confirmed by analytical simulations, as shown in Fig. 2, for coplanar electrodes with parameters $\mathbf{T} = 4.17\,\mu$m. The impact of the distance between the electrode and the edge of the sample $\mathbf{g_h}$ is also examined. For $\mathbf{g_h} \geq 0.5 \times \mathbf{h_{med}}$, we notice that the capacity is maximal with a constant value. Furthermore, when $\mathbf{g_h} > \mathbf{T}$, $\mathbf{g_h}$ has no more impact on the electrodes' capacitance.

Simulations confirm that Eq. (3) can be used as an approximation for the capacitance and allow for determining an optimal thickness for the two electrodes.

The maximum capacitive signal can be obtained by minimizing the gap $\mathbf{g}$ while modeling electrodes, the width of which is comparable to the thickness of the solution. In opposition to parallel plates capacitors, the capacitance does not increase in proportion to $\mathbf{w/a}$, but proportionally to $\ln(\mathbf{w/a})$.
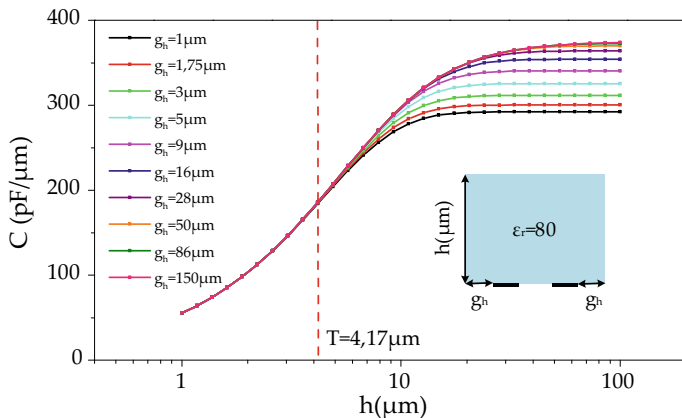

Fig. 2 Capacitance as a function of $\mathbf{h_{med}}$ and $\mathbf{g_h}$

2.2 Interdigitated Electrode Modeling

2.2.1 Semi-layer Capacitance Calculation

The analytical study of interdigitated electrodes allows for determining the essential geometrical parameters for optimization and how they influence the response of the biosensor. The structure of coplanar interdigitated electrodes is given in Fig. 3a. It can be considered as the concatenation of unitary symmetric coplanar electrodes forming fingers. These fingers have the same width **w** and are separated by an interval **g**. The length **L** is generally large enough to neglect the side effect of the electric field.

The capacitance of unitary cells (**C_I/C_E**) can be expressed according to **k^c_{cell}**, the unit cell factor. **k^c_{cell}** depends on three parameters: the metalization ratio **η**, the periodicity of electrodes **λ** [14], and the ratio of height/width **r** defined by Eqs. (4) and (5). The parameter **λ** depends on **w** and **g**.

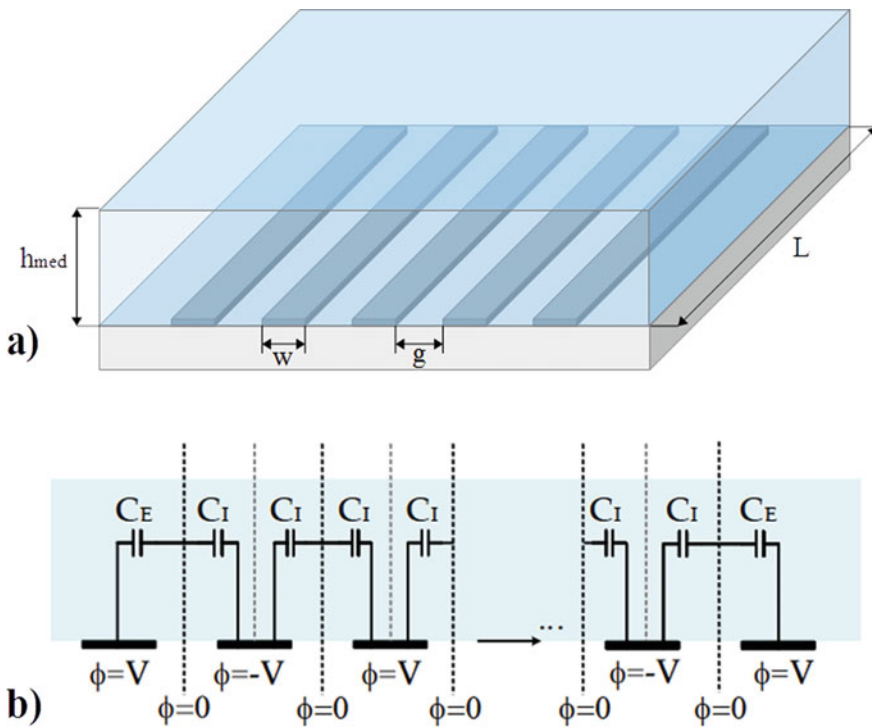$$\eta = \frac{w}{w+g} = \frac{2w}{\lambda} \tag{4}$$

Fig. 3 Diagram of interdigitated electrodes

$$r = \frac{2h_{med}}{w + g} \tag{5}$$

Using corresponding techniques of a conformal map (or angle-preserving), one can determine the internal and external capacitances of coplanar electrodes [15]. The equivalent electrical circuit for a configuration of **N** electrodes is shown in Fig. 3b. To simplify the model, we assume that the electrodes are sufficiently long to maintain a relatively constant electric field along the electrodes. Therefore, the capacitance of a single layer could be considered to be the association of two capacities: $\mathbf{C_I}$, which is the half-capacitance between the internal electrode and the reference ($\mathbf{V_{ref}} = 0$), and $\mathbf{C_E}$, which is the capacitance between an external electrode and the substrate. The total capacitance of a single layer is thus given by:

$$C = (N - 3)\frac{C_I}{2} + 2\frac{C_I C_E}{C_I + C_E} \tag{6}$$

If **N** < 4, the capacitance of a two-cell structure becomes **C = C_E/2**. $\mathbf{C_I}$ and $\mathbf{C_E}$ can be calculated as follows.

$$C/L = \varepsilon_0 \varepsilon_{r,med} K_{cell}(\eta, h_{med}) \tag{7}$$

where $\mathbf{\varepsilon_0}$ is the vacuum permittivity, $\mathbf{\varepsilon_{r,med}}$ the relative permittivity of the sample medium, and $\mathbf{k^c_{cell}}$ is the geometric factor. $\mathbf{k^c_{cell}}$ can be calculated in the case of coplanar electrode configuration using Jacobi's elliptic equations [12], as shown in Table 1. This technique uses the method of partial capacitances for a multilayer dielectric material with the calculation of partial parallel capacitance (**PPC**) and partial series capacitance (**PSC**) for each layer. In the case of a semi-infinite layer ($\mathbf{h_{med} \gg T}$), as here, the model is simpler and consists of calculating only one capacitance.

To verify the analytical expression of the capacitance for interdigitated electrodes, simulations were performed using FEM with COMSOL Multiphysics software and AC/DC modules. The capacitance (**C**) is determined as follows: **C = Q/V** (where Q is the electric charge and V the electric potential). Three sets of simulations were done, and results are given in Fig. 4a–c.

First, simulations were performed by varying $\mathbf{\varepsilon_{r,med}}$ from 1 to 100, for two numbers of electrodes (**N** = 10 and 20) by keeping $\mathbf{\eta}$ to 0.5. They were performed considering a semi-infinite layer: $\mathbf{h_{med} \rightarrow \infty}$ for analytical models and $\mathbf{h_{med} \gg T}$ for FEM simulations.

Second, simulations were performed by varying the electrodes' periodicity $\mathbf{\lambda}$ for 8 layer heights by keeping $\mathbf{\eta}$ to 0.5, $\mathbf{\varepsilon_{r,med}}$ to 80, and using the semi-finite $\mathbf{k^c_{cell}}$ coefficient. These results demonstrate that the impact of the sample height can be neglected if it is at least two times higher than the electrodes' periodicity. Ninety-nine percent of the injected signal power is concentrated in the first **2λ** depth. This property allows for controlling the penetration depth of the electric field of interdigitated electrodes by fixing $\mathbf{\lambda}$.

Table 1 K^c_{cell} equations for a semi-infinite and semi-finite layer

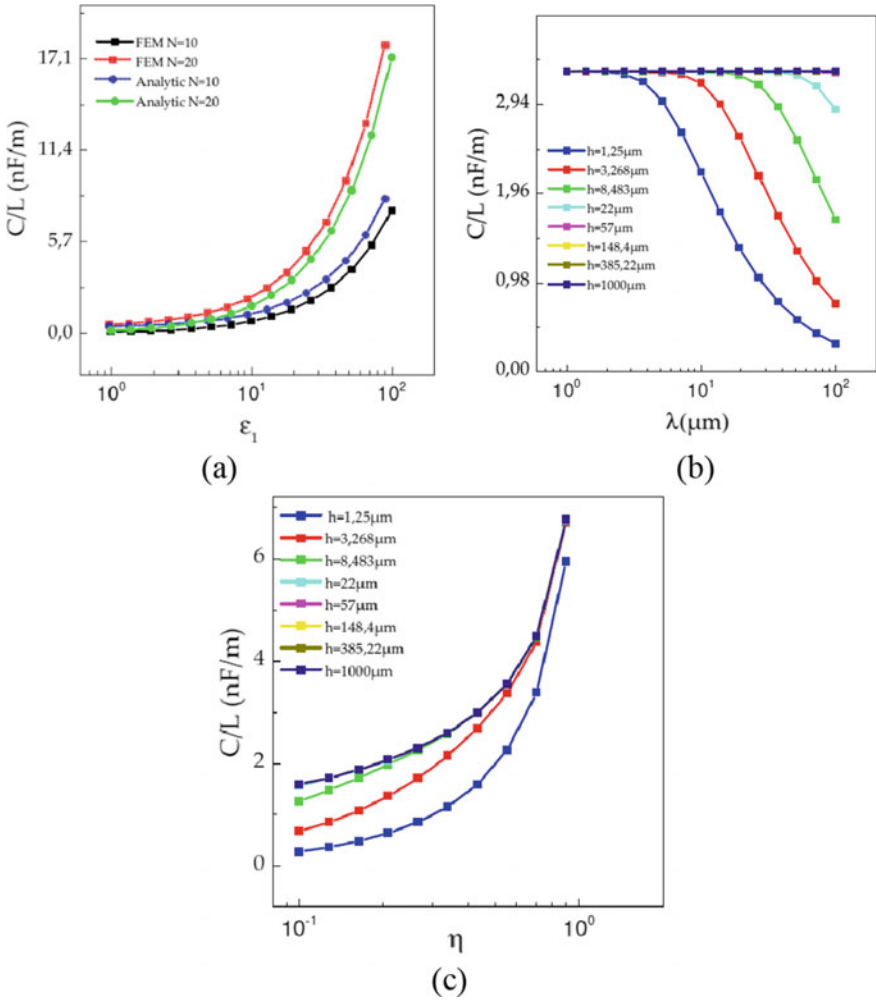|	C_I		C_E	
	PSC	PPC	PSC	PPC
$h < \infty$	$\kappa^c_{cell} = \dfrac{K(k_{I,CPS'})}{K(k_{I,CPS})}$ $k_{I,CPS} = t_2$	$\kappa^c_{cell} = \dfrac{K(k_{IP,PPC'})}{K(k_{IP,PPC})}$ $k_{I,PPC} = \sqrt{\dfrac{(t_4^2 - 1)}{(t_4^2 - t_2^2)}}$	$\kappa^c_{cell} = \dfrac{K(k_{E,CPS})}{K(k_{E,CPS'})}$ $k_{E,CPS} = \sqrt{\dfrac{(t_4 - t_3)}{(t_4 - 1)}}$	$\kappa^c_{cell} = \dfrac{K(k_{E,PPS'})}{K(k_{E,PPS})}$ $k_{E,PPC} = \dfrac{1}{t_3}\sqrt{\dfrac{(t_4^2 - t_3^2)}{(t_4^2 - 1)}}$
	$t_2 = sn(K(k_1)(2\eta - 1), k_1^2)$ $t_4 = \dfrac{1}{k_I}$ $k_I = \left(\dfrac{\vartheta_2(0,q)}{\vartheta_3(0,q)}\right)^2$ $k'_I = \sqrt{1 - k_I^2}, \ q = e^{-2\pi r}$		$t_4 = \cosh\left(\dfrac{\pi(1+\eta)}{4r}\right)$ $t_3 = \cosh\left(\dfrac{\pi(1-\eta)}{4r}\right)$ $k_{E,CPS/PPC'} = \sqrt{1 - k_E^2}$	$t_4 = \cosh\left(\dfrac{\pi(1+\eta)}{8r}\right)$ $t_3 = \cosh\left(\dfrac{\pi(1-\eta)}{8r}\right)$
$h = \infty$	$\kappa^c_{cell} = \dfrac{K(k')}{K(k)}$ $k = \sin(\dfrac{\pi}{2}\eta)$ $k' = \sqrt{1 - k^2}$		$\kappa^c_{cell} = \dfrac{K(k')}{K(k)}$ $k = \dfrac{2\sqrt{n}}{1+n}$ $k' = \sqrt{1 - k^2}$	

Fig. 4 FEM and analytical evaluation of linear capacitance (C/L) as a function of **a** the relative permittivity of the sample $\varepsilon_{r,med}$, **b** electrode periodicity λ, and **c** the metalization ratio η

The third set of simulations was performed by varying the metalization ratio η from 0.1 to 0.9 for 8 layer heights by keeping $\varepsilon_{r,med}$ to 80. Capacitance increases with η, which can be explained by the increase of electrode surfaces and the decrease in the gap between the electrodes. For a higher value of η, the impact of the sample thickness becomes less significant due to the decreasing of W_{eff}, reducing the penetration depth T at the same time.

2.2.2 Two-Layer Capacitance Calculations

In real interdigitated sensors, the capacitive effect appears not only in the sample direction but also in the substrate. The total capacitance is composed of the addition of sample capacitance (or air in case of open measurement without samples) and the substrate capacitance. The impact of this capacitance must be considered and evaluated. Its calculation is similar to the sample calculation using $\mathbf{K^c_{cell}}$ factors. $\mathbf{K_{cell}}$ is the geometrical sensor factor, which depends on the unitary $\mathbf{K^c_{cell}}$ factors and the number of electrodes. The substrate thickness is generally high compared to λ, and the equation for a semi-infinite medium is used. To analyze the impact of the substrate, analytical simulations were performed using Eqs. (8) to (10) with the following parameters: $\boldsymbol{\varepsilon}_{\mathbf{r,substrate}} = 4.07$ (relative permittivity of the glass), $\boldsymbol{\varepsilon}_{\mathbf{r,air}} = 1$, $\boldsymbol{\varepsilon}_{\mathbf{r,sample}} = 80$ (relative permittivity of pure water), $\boldsymbol{\eta} = 0.5$, $\mathbf{w} = 3\ \mu\text{m}$, $\mathbf{h_{substrate}} = 1\ \text{mm}$, $\mathbf{L} = 1\ \text{mm}$ and $\mathbf{h_{med}} = 1\ \text{mm}$. Results are presented in Fig. 5 for air and the sample.

In the case of an open configuration (without a sample), the impact of the substrate capacitance is higher than the effect of the sensing side. If the ratio of relative permittivity between the sample and the substrate is high, the contribution of the substrate stays small, as shown in Fig. 5b. That is why a low-permittivity substrate is more suitable for impedance-based sensors. For example, a silicon substrate has a relative permittivity approximately two to three times higher than glass substrates.

$$C_{substrate} = \left(\varepsilon_0 \varepsilon_{r,substrate}\right) \times \left[\left((N-3)\frac{C_I}{2}\right) \times \left(\frac{2C_I C_E}{C_I + C_E}\right)\right] \tag{8}$$

$$C_{sample} = \left(\varepsilon_0 \varepsilon_{r,sample}\right) \times \left[\left((N-3)\frac{C_I}{2}\right) \times \left(\frac{2C_I C_E}{C_I + C_E}\right)\right] \tag{9}$$
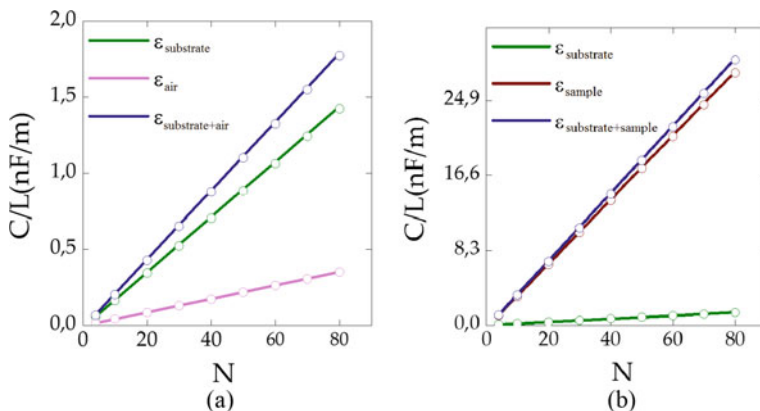

Fig. 5 Impact of the relative substrate permittivity on the global capacitance for a glass substrate **a** without a sample, and **b** with a water-based sample

$$C_{substrate+sample} = \left(\varepsilon_0\left(\varepsilon_{r,substrate} + \varepsilon_{r,sample}\right)\right) \times \left[\left((N-3)\frac{C_I}{2}\right) \times \left(\frac{2C_I C_E}{C_I + C_E}\right)\right] \tag{10}$$

2.2.3 R//C Equivalent Model for Liquid Samples

As biological samples are mainly composed of water, impedance data is commonly analyzed using an **R//C** parallel-based equivalent circuit as a reference. **R_{med}** and **C_{med}** parameters represent the effects of electrical conductivity and electrical permittivity of the sample medium, respectively. The capacitances of the previous analytical model (upper layer) are now replaced by impedance (or admittance) of the sample medium using Eqs. (11) to (13). The factor **K_{cell}** remains the same as before.

$$\underline{Y}_{med} = G_{med} + jB_{med} = \frac{1}{R_{med}} + j\omega C_{med} \tag{11}$$

with

$$C/L = \varepsilon_0 \varepsilon_{r,med} K_{cell} \tag{12}$$

$$R_{med} \times L = \frac{1}{\sigma_{med} K_{cell}} \tag{13}$$

This model presents a cutoff frequency **$f_{c,HF}$**, due to the couple **R_{med}//C_{med}**. According to Eqs. (12) and (13), **$f_{c,HF}$** does not depend on the electrode geometry but only on the electric and dielectric properties of the sample, as calculated in Eq. (14).

$$f_c = \frac{1}{2\pi RC} = \frac{\sigma_{med}}{2\pi \varepsilon_{med}} \tag{14}$$

To prove this assumption, both analytical and FEM simulations were made with the same sample for two different interdigitated electrode sensors (**C_{S1}** and **C_{S2}**) with the geometrical parameters resumed in Table 2.

These two sensors were simulated in the presence of a solution (modeled by a parallel piped rectangle) of a semi-infinite thickness, with an electrical conductivity

Table 2 Geometrical parameters for sensors C_{S1} and C_{S2}

	N	η	w (μm)	g (μm)	K_{cell} (m^{-1})
C_{S1}	40	0.5	3	3	0.97
C_{S2}	40	0.6	30	20	1.1561

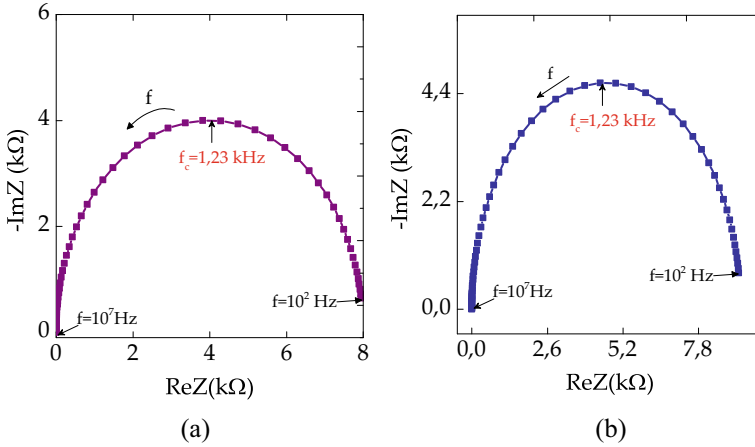**Fig. 6** Nyquist and Bode diagram for simulated sensors C_{S1} and C_{S2} with analytical models (lines) and FEM (rectangles)

of 1 µS/cm and a relative permittivity of 80. Figure 6a and b represent the Nyquist diagram for C_{S1} and C_{S2} sensors, respectively. The Figures demonstrate that the cutoff frequency does not vary for the two geometries: $\mathbf{f_{c,HF}} = 1.23$ kHz. One can see that the analytical model provides results that are in perfect cohesion with the FEM simulation results.

2.2.4 Electrical Double Layer

When a metal electrode is immersed in an electrolyte, a double layer is formed at the interface between the electrode and the electrolyte. As is well known, the double layer acts as a barrier for measurements at low frequencies (<1 MHz). Thus, the determination of its thickness is a paramount parameter. Double layer effects allow us to evaluate the measurement band, optimize the geometrical parameters, and correctly determine the global equivalent circuit model.

The double-layer capacitance is composed of several contributions and is generally represented by the compact layer of "Helmholtz" or "Stern" [16, 17]. Its structure is completed by a "diffusion" layer, composed of electrostatically attracted elements at a distance from the surface of the electrode. The total thickness of the double layer can be defined as the outer limit of the "diffusion" layer that separates it from the solution [18, 19].

The thickness of the double layer induces an electrochemical potential difference between the solution and the electrode. The total capacitance of the double layer $\mathbf{C_{DL}}$ is composed of a combination of the compact layer capacitance of Helmholtz (C_H) and the diffusion layer capacitance (C_D), which can be calculated using Eqs. (15) to (18).

$$\frac{1}{C_{DL}} = \frac{1}{C_H} + \frac{1}{C_D} \tag{15}$$

with

$$C_H = \frac{\varepsilon_0 \varepsilon_r}{L_H} \tag{16}$$

$$C_D = \frac{\varepsilon_0 \varepsilon_r}{\lambda_{DEBYE}} \cosh(\frac{zeV}{4K_BT}) \, C_D \approx \frac{\varepsilon_0 \varepsilon_r}{1.5\kappa^{-1}} \tag{17}$$

$$\kappa^{-1} = \sqrt{\frac{\varepsilon_0 \varepsilon_r K_B T}{2 \times 10^3 n_j z_j^2 e^2}} \tag{18}$$

where λ_D represents the Debye length, K_B the Boltzmann constant, T the absolute temperature, z_j the charge amplitude of each "j" ion, e the elementary charge, and n_j the molar concentration of each "j" ion. This phenomenon (the formation of an electric double layer) occurs on each electrode. One can see this in the model shown in Fig. 7, which gives an equivalent circuit for an interdigitated structure and an example of an equivalent circuit for $N = 4$. R_E and R_I represent the conductive effects of the medium on each interior and exterior electrode.

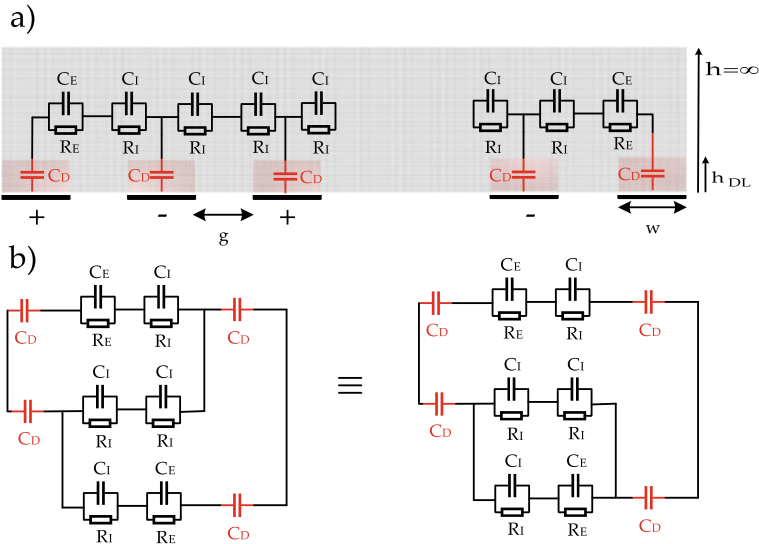The total impedance of the equivalent circuit shown in Fig. 7 can be calculated as follows, using Eqs. (19) to (23):

Fig. 7 **a** Electrical equivalent circuit for the interdigitated structure of N electrodes, and **b** an example of four electrodes

$$Y_T = \frac{1}{Z_{i1}} + \frac{(N/2) - 1}{Z_{i,\text{sup}}} + \frac{N - 1}{Z_L} \tag{19}$$

With

$$Z_{i1} = Z_i + 2Z_{DL,i} \tag{20}$$

$$Z_{i,\text{sup}} = \frac{Z_i}{2} + 2Z_{DL,i} \tag{21}$$

$$Z_L = Z_{Sol,L} + 2Z_{DL,L} \tag{22}$$

$$Z_{DL,i} = \frac{1}{j\omega C_{DL,i}} \,;\, Z_i = \frac{2R_i}{1 + j\omega R_i C_i} \,;\, Z_{DL,L} = \frac{1}{j\omega C_{DL,L}} \,;\, Z_{Sol,L} = \frac{R_{sol,L}}{1 + j\omega R_{sol,L} C_{sol,L}} \tag{23}$$

When $\omega \to 0$ (at very low frequencies):

$$\underset{\omega \to 0}{Lim} \, \text{Im}(Y_T)/\omega = \underset{\omega \to 0}{Lim} \, C_T = \frac{1}{4}(2C_{DL,L}(N - 1) + C_{DL,i}) \tag{24}$$

$$\underset{\omega \to 0}{Lim} \, \text{Re}(Z_T) = \frac{2C_{DL,i}^2 R_i(2 + N) + 4C_{DL,L}^2 R_{sol}(N - 1)}{(2C_{DL,L}(N - 1) + NC_{DL,i})^2} \tag{25}$$

When $\omega \to \infty$ (at higher frequencies):

$$\underset{\omega \to \infty}{Lim} \, C_T = \frac{1}{2}\left(\frac{2C_{DL,L}C_{sol}(N - 1)}{C_{DL,L} + 2C_{sol}} + \frac{2C_{DL,i}C_i(C_{DL,i}(N - 1) + C_i N)}{(C_{DL,i} + C_i)(C_{DL,i} + 2C_i)}\right) \tag{26}$$

$$\underset{\omega \to \infty}{Lim} \, \text{Re}(Z_T) = 0 \tag{27}$$

The double-layer capacity induces a second cutoff frequency at a low frequency, $f_{c,LF}$. This effect can completely predominate the measurements and must be studied before fabrication of the electrodes and their optimization, if necessary. The cutoff frequency can be calculated using Eq. (28), as follows:

$$f_{c,BF} = \frac{1}{2\pi \underset{\omega \to 0}{Lim} Z_T \underset{\omega \to 0}{Lim} C_T} \tag{28}$$

$$f_{c,BF} = \frac{2C_{DL,L}(N - 1) + NC_{DL,F}}{\pi R_i C_{DL,F}^2(N + 2) + 2\pi R_{S,L} C_{DL,L}^2(N - 1)}$$

The impact of C_{DL} at a high cutoff frequency can be calculated using Eq. (29):

$$f_{c,HF} = \frac{1}{2\pi R_T \underset{\omega \to \infty}{Lim} C_T} \tag{29}$$

$$f_{c,HF} = \frac{(2C_{DL,L}(N-1) + NC_{DL,F})^2}{\pi X \left(2C_i^2 R_i(N+2) + 4C_{DL,L}^2 R_{S,L}(N-1) \right)}$$

$$X = \left(\frac{2C_{DL,L}C_{S,L}(N-1)}{C_{DL,L} + 2C_{S,L}} + \frac{C_{DL,F}C_i(C_{DL,F}(N-1) + NC_i)}{(C_{DL,F} + C_i)(C_{DL,F} + 2C_i)} \right)$$

In most cases, $\mathbf{C_{DL}}$ is very high compared to capacitance induced by water permittivity and has no significant impact. In this case, the cutoff frequency only depends on $\mathbf{C_I/R_I}$ and $\mathbf{C_E/R_E}$, and can be assimilated to Eq. 14.

3 Interdigitated Sensor Optimization

In this section, the effect of each parameter in the global impedance spectrum is analyzed to optimize interdigitated sensors according to the targeted application. The electrodes' wavelength $\mathbf{\lambda}$ is not reviewed in this section. This parameter (depending on $\mathbf{w}$ and $\mathbf{g}$) is used to evaluate the penetration depth and was already considered in the previous section. To evaluate the impact of the electrode width and gap, it is more suitable to use another indicator as the metalization ratio $\mathbf{\eta}$.

3.1 Effect of the Number of Electrodes

As before, simulations were performed to study the impact of geometrical parameters on the global impedance spectrum (module and phase) to optimize interdigitated sensors.

First, simulations were performed using both analytical and FEM models by varying the number of electrodes from 10 to 80 by a step of 10. The other parameters were set at $\mathbf{\eta} = 0.5$ and $\mathbf{w} = \mathbf{g} = 10$ µm. The thickness of the double layer was calculated using Eq. (15), with $\mathbf{\lambda_D} = 80$ nm. The liquid sample was considered with an infinite thickness ($\mathbf{h_{med}} \gg \mathbf{\lambda}$), with $\mathbf{\varepsilon_{r,med}} = 80$ and $\mathbf{\sigma_{med}} = 1$ µS/cm.

Results are displayed in Fig. 8, with a Bode diagram for module and phase, from which the real part and capacitance are deduced. Both FEM and analytical results are in concordance, demonstrating the validity of the analytical model. One can see that $\mathbf{N}$ does not have a significant impact on the phase and cutoff frequencies, as shown in Fig. 9. The low impact observed for the low number of electrodes is due to the peripheral electrodes and became negligible when the number of electrodes was higher than 20. One can conclude that the number of electrodes may influence only by reducing the value of the impedance. This parameter can be used in experimental measurement to adapt the impedance to the desired range to be compatible, for example, with an impedance analyzer.
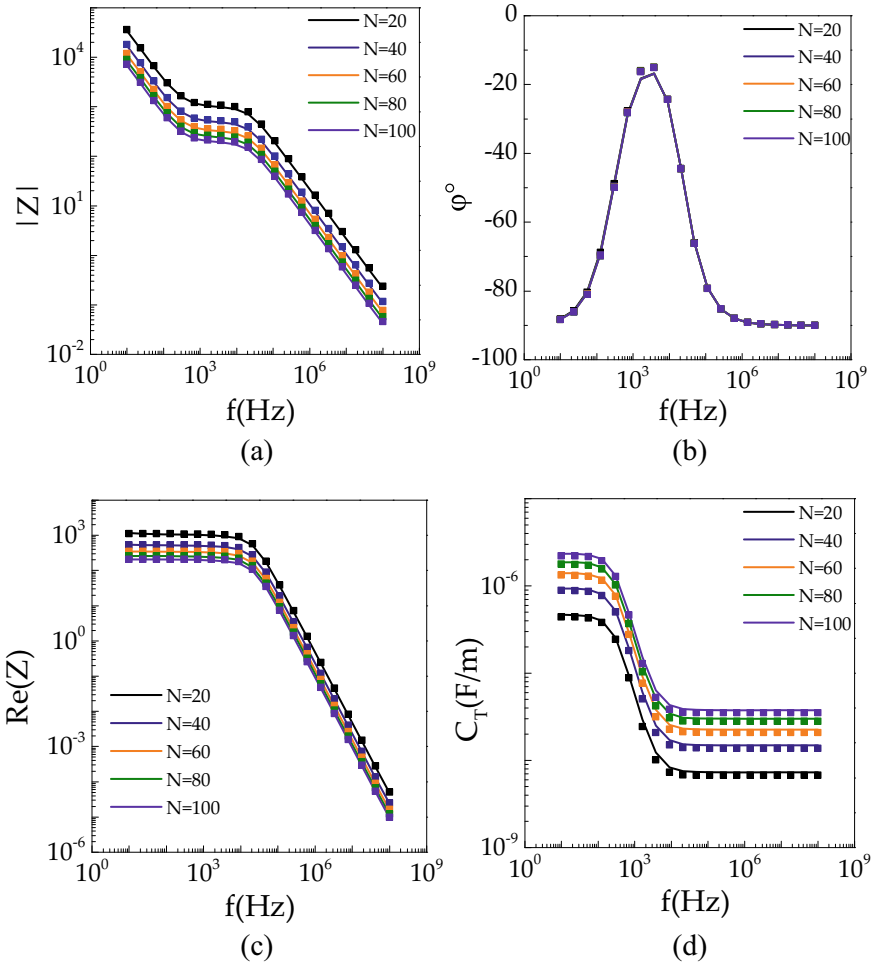
Fig. 8 Bode diagram for analytical (line) and FEM (points) simulations as a function of the number of electrodes N. Diagrams show **a** module, **b** phase, **c** real part, and **d** capacitance extraction

3.2 Effect of the Metalization Ratio

Other simulations were performed to study the impact of the metalization ratio η. The number of electrodes **N** was set to 20 and **h** to 4 mm (to consider a semi-infinite layer). η is a function of two other parameters, namely the electrode width **w** and the electrode gap **g** (Eq. 4). Thus, simulations were performed by fixing one of the **w** | **g** parameters and varying the other, and by fixing η and analyzing the impact of one of the **w** | **g** parameters.
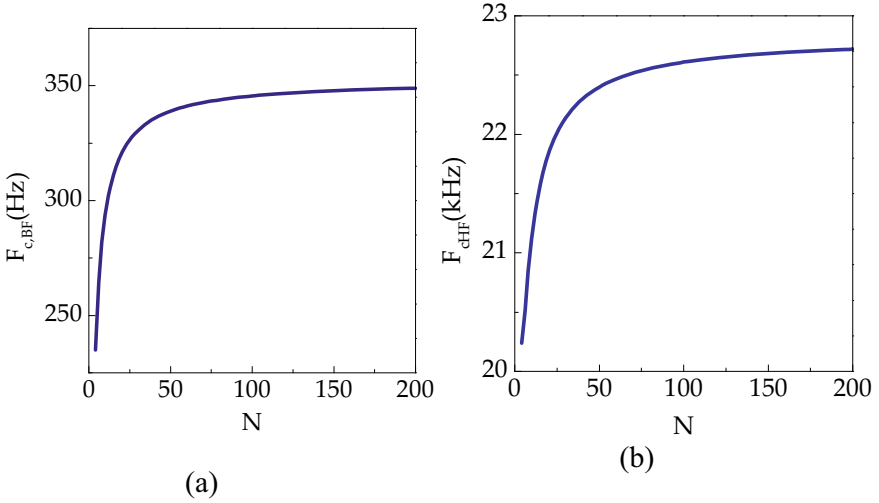
Fig. 9 High and low cutoff frequencies as a function of the number of electrodes N

In a first step, the electrode width **w** was set to 10 μm, and the electrode gap **g** was varied to obtain a metalization ratio η varying from 0.1 to 0.9, using Eq. (30).

$$g = \frac{w(1 - \eta)}{\eta} \qquad (30)$$

The results are presented in Fig. 10. A decrease in **g** causes an increase in the ratio η, resulting in a logarithmic increase of $f_{c,LF}$, which implies a diminution of the useful bandwidth (between $f_{c,LF}$ and $f_{c,HF}$). C_{DL} is not impacted because it only depends on the electrode surface (**w**, **L**), and the sample impedance increases as a function of the logarithmic relation of the **g/w** ratio.

In Fig. 11, the influence of **g** for an η-maintained constant was studied. For a fixed value of η, increasing **g** implies increasing **w**. Since C_{DL} is proportional to **w**, and impedance depends on the logarithmic relation of **g/w**, we obtain a logarithmic decrease of $f_{c,LF}$ with increasing **g**. There is no significant impact on $f_{c,HF}$, because it mainly depends on the sample's intrinsic properties, as explained previously in the "Electrical double layer" section. When η > 0.7, the electrodes are very close to each other, and the simplified model is no longer valid (see Eq. 3). The electric field is concentrated in a volume that is too confined.

In a second step, the electrode gap **g** was set to 10 μm, and the electrode width **w** was varied to obtain a metalization ratio η from 0.1 to 0.9, using Eq. (31):

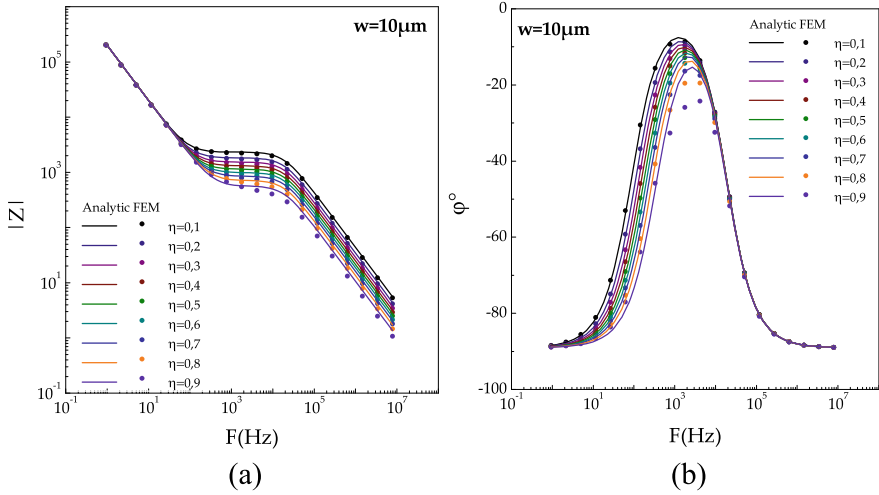$$w = \frac{\eta g}{(1 - \eta)} \qquad (31)$$

Fig. 10 Simulated impedance as a function of η by setting **w** to 10 µm using the analytical model (lines) and FEM (points). **a** Impedance module, and **b** impedance phase
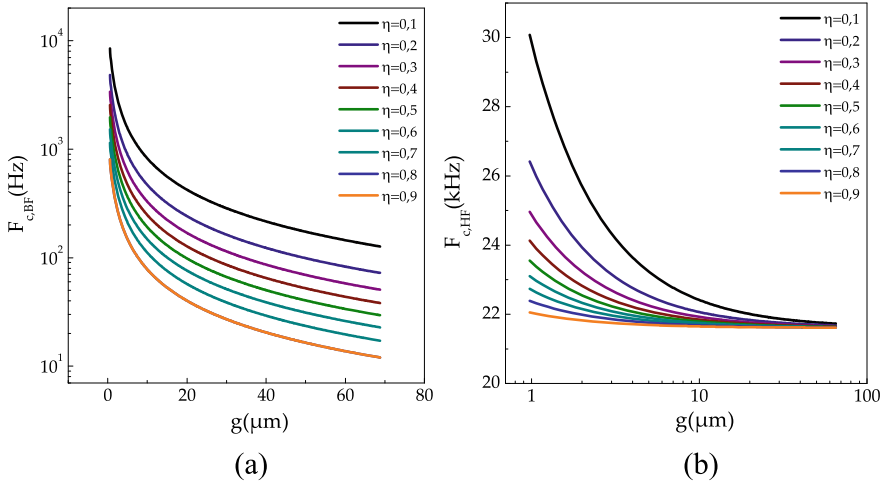

Fig. 11 Simulated cutoff frequencies as a function of **g** for different η values using the analytical model (lines) and FEM (points). **a** Low cutoff frequency, and **b** high cutoff frequency

Results are shown in Fig. 12. The increasing of ratio η, due to the increase of **w**, causes a logarithmic increase of $f_{c,LF}$, implying a diminution of the useful bandwidth (between $f_{c,LF}$ and $f_{c,HF}$). C_{DL} is proportional to **w** because it depends on the electrode surface (**w, L**). The sample impedance increases as a function of the logarithmic relation of the **g/w** ratio.
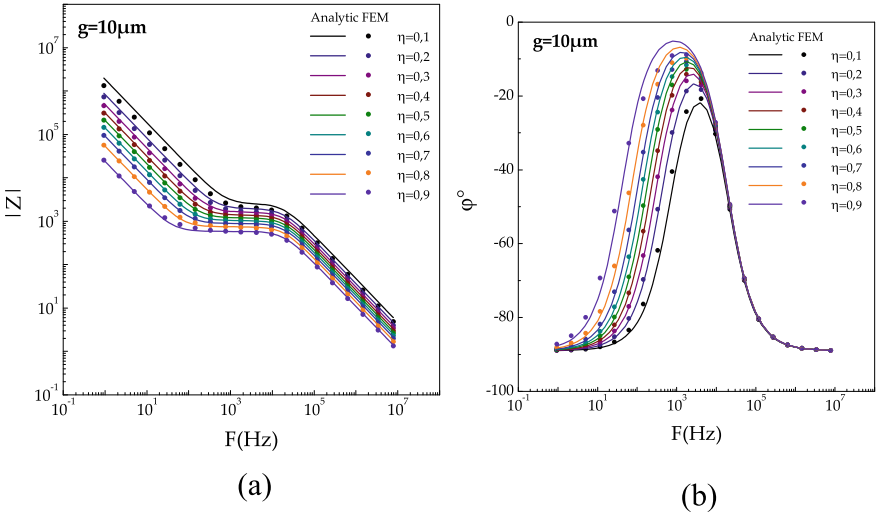
Fig. 12 Simulated impedance as a function of **η** by setting **g** to 10 µm using the analytical model (lines) and FEM (points). **a** Impedance module, and **b** impedance phase

In Fig. 13, the impact of **w** with constant **η** was studied. With a constant **η**, increasing **w** implies an increase of **g**. As C_{DL} is proportional to **w**, and impedance depends on the logarithmic relation of **g/w**, we obtain a logarithmic decrease in $f_{c,LF}$ with increasing **g**. There is no significant effect on $f_{c,HF}$, as it chiefly depends on the sample's intrinsic properties, as explained above in the "Electrical double layer"
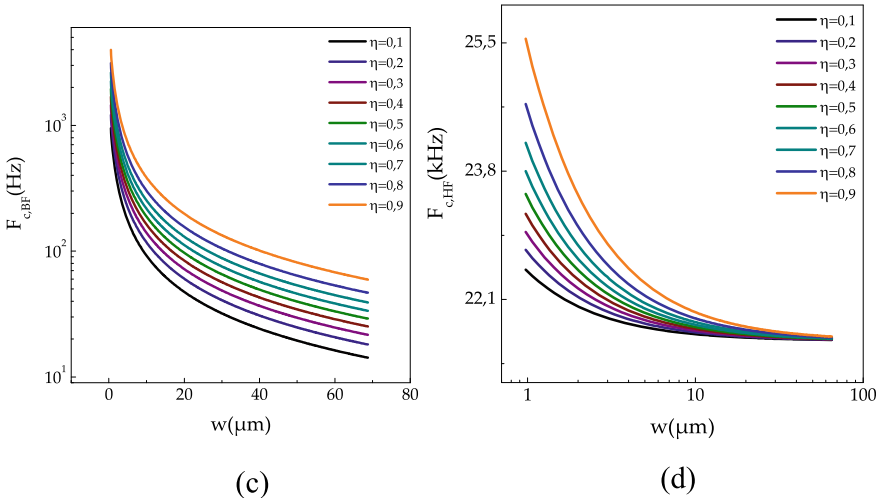

Fig. 13 Simulated cutoff frequencies as a function of **w** for different **η** values using the analytical model (lines) and FEM (points). **a** Low cutoff frequency, and **b** high cutoff frequency

section. When $\eta > 0.7$, the electrodes are quite close to each other, the simplified model is no longer valid (see Eq. 3), and the electric field is concentrated in too confined a volume.

From the results of Figs. 10, 11, 12 and 13, one can conclude that the metalization ratio can efficiently contribute to a reduction of the double-layer effect and increase the useful frequency band when **g** or **w** are increased. Under these conditions, it is more suitable not to choose too high or too low a ratio of η to keep a good electric field distribution. $\eta = \mathbf{0.5}$ (**g** = **w**) provide the most uniform electric field distribution between the interdigitated electrodes.

3.3 Effect of Substrate Capacitance

The electrical effect of the substrate ($\mathbf{Z_S}$) is mainly due to its permittivity, ranging from 2 to 14 (relative), depending on the material used, as seen in Table 3. Substrate electrical conductivity is generally very low and neglected. Substrate permittivity adds a capacitive semi-layer in parallel with the characteristic impedance of the biosensors. Global impedance $\mathbf{Z_T}$ can be calculated using Eqs. (32) and (33). Substrate impedance is calculated using the same $\mathbf{K_{cell}}$ factor as for sample impedance. Due to the low relative permittivity of substrate materials compared to water, its capacitance effect occurs at higher frequencies and has only an impact on $\mathbf{f_{c,HF}}$, as shown in Eq. (34). If the relative permittivity of the substrate is low compared to the sample permittivity, the decrease in $\mathbf{f_{c,HF}}$ remains minimal. For example, a relative glass permittivity of 4.7 induces a decrease in $\mathbf{f_{c,HF}}$ of only 6%, as compared to $\mathbf{f_{c,HF}}$ calculated without taking into account glass permittivity. Glass substrate is transparent, resistant to numerous solvents, stable, easy to handle for processing, biocompatible, cheaper than other substrates, and presents a low relative permittivity. For that, it is the more suitable material to use for the substrate.

$$Y_T = \frac{1}{Z_{i1}} + \frac{(N/2) - 1}{Z_{i,\text{sup}}} + \frac{N - 1}{Z_L} + \frac{N - 1}{Z_S} \tag{32}$$

Table 3 Electrical relative permittivity and conductivity of different substrate materials

Material	Relative electrical permittivity	Electrical conductivity (σ/m)
PTFE	2.1	$<10^{-9}$
PMMA	2.6 to 3.12 (room temperature)	$<10^{-9}$
Polyimide	3.4	$<10^{-9}$
Glass	3.7 to 10	$<10^{-9}$
Amorphous silicon	11.8	3.10^{-5}

$$Z_S = \frac{2R_{Sub}}{1 + j\omega R_{Sub}C_{Sub}} \tag{33}$$

$$F_{C,H} = \frac{1}{2\pi R_T C_T} F_{C,H} = \frac{1}{2\pi R_T C_T} \tag{34}$$

with

$$R_T = \frac{R_{sol}R_{sub}}{R_{sol} + R_{ssub}} \approx R_{sol} \text{ and } C_T = C_{sol} + C_{sub} \tag{35}$$

To verify the previous equations, FEM simulations were executed for an interdigitated sensor with a semi-infinite substrate and a relative permittivity of four on the bottom face. A semi-infinite sample employed a relative permittivity of 80 and a conductivity of 100 µS/cm for the upper face. Results are shown in Fig. 14 for both the analytical model calculation and the FEM simulation. One can conclude that the analytical results for the equivalent circuit model are in concordance with the FEM simulations.
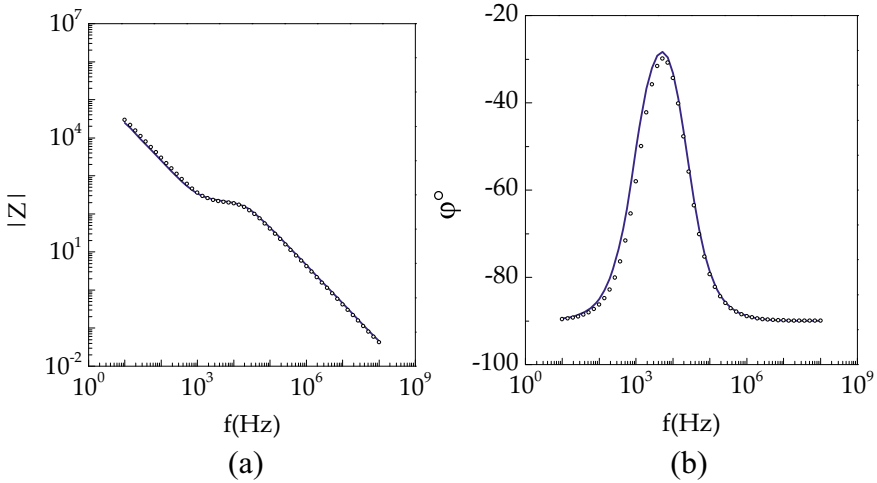

Fig. 14 Results of the analytical evaluation and FEM simulations of an interdigitated sensor with a liquid sample and a glass substrate. Bode diagram for **a** module, and **b** phase

3.4 Optimization Methodology

BIA sensor optimizations are mainly focused on bandwidth improvement, which needs to be wide enough to observe all the useful frequency bands of the sample. For biological samples, useful frequencies are centered around the β dispersion zone. One decade before and after this zone is generally sufficient to characterize a bio sample. These frequencies depend on sample complex conductivity ($\sigma_{samp}(\omega)$) and can be estimated using the impedance database [20] or models such as Maxwell mixture theory (MMT) [21] or Cole–Cole [22], for example.

Another typical parameter for optimization of interdigitated sensors is the depth of penetration. By varying the parameter λ, it is possible to set the sample thickness desired for analysis. This optimization is particularly interesting when one wants to characterize a thin sample, as for surface cell cultures or cell settling, for example.

The last optimization concerns the impedance range. Low-cost or embedded impedance measurement devices are generally limited in their impedance range and require a sensor with an adapted response.

A better optimization consists of determining the optimum compromise between frequency band, impedance range, and penetration depth. To achieve this, we propose the following methodology:

1. Use a database or models to evaluate the complex conductivity $\sigma_{samp}(\omega)$ of the samples to characterize.
2. Set the parameter λ as a function of the desired penetration depth, with a metalization ratio η of 0.5 ($\mathbf{w} = \mathbf{g}$).
3. Use equations of previous sections with the complex permittivity of samples to check if the bandwidth is correct. Since the number of electrodes $\mathbf{N}$ and electrodes length $\mathbf{L}$ have no impact on the bandwidth, their value can be set arbitrarily for this step.
4. If the bandwidth is insufficient, the metalization ratio η can be increased by keeping λ constant. It is recommended not to use too high a value of η in order to maintain a correct electric field distribution.
5. If the previous optimization is insufficient, increase the parameter λ to obtain the appropriate bandwidth. This operation reduces the sensitivity by using a penetration depth higher than needed but permits observation of all the useful sample spectrum. This step consists of selecting the best compromise between sensitivity and bandwidth.
6. Set numbers of electrodes $\mathbf{N}$ and length $\mathbf{L}$ to obtain the desired impedance range. It is recommended to use at least 20 electrodes to reduce the effect of outside electrodes on global impedance.

4 Experimentation

To verify our assumption, different sensor designs were fabricated and characterized using biological samples. Various $\mathbf{N}$, $\mathbf{w}$, and $\mathbf{g}$ values were tested to validate

their impact on the global impedance spectrum. All measurements of this section were performed at room temperature (23 °C $\pm$ 1 °C) using an impedance analyzer (E4990A, Keysight Technologies).

4.1   Samples Choices and Modeling

Thus far this work has focused on interdigitated sensor modeling and optimization without discussing the influence of the biological species. To accomplish this, we chose yeast cells (*Saccharomyces cerevisiae*) as a biological model because it is one of the most commonly studied cells. Yeast cells are simple to manipulate, resistant to many ionic concentrations, not pathogenic, and easy to dilute to obtain the appropriate concentration. Deionized water and two calibrated ionic solutions (1314 μS/cm and 5000 μS/cm at 25 °C) were used as references for our measurements. Deionized water, with its very low conductivity, is well suited to serve as a reference for electrical permittivity measurements (78 for pure water).

A yeast cell sample can be modeled by its complex conductivity using MMT, as in Eqs. (36) and (37). Calibrated solutions can be readily modeled using the given conductivity and the relative permittivity of water ($\varepsilon_{r,water} \approx 78$), as shown in Eq. (40).

$$\frac{\frac{\sigma_{samp}(\omega)}{\sigma_{elec}(\omega)} - 1}{\frac{\sigma_{samp}(\omega)}{\sigma_{elec}(\omega)} + 2} = \rho_V \frac{\frac{\sigma_{cell}(\omega)}{\sigma_{elec}(\omega)} - 1}{\frac{\sigma_{cell}(\omega)}{\sigma_{elec}(\omega)} + 2} \tag{36}$$

$$\sigma_{cell}(\omega) = \sigma_{mem}(\omega) \frac{\left(2\sigma_{mem}(\omega) + \sigma_{cyt}(\omega)\right)r_{ext}{}^3 - 2\left(\sigma_{mem}(\omega) - \sigma_{cyt}(\omega)\right)r_{int}{}^3}{\left(2\sigma_{mem}(\omega) + \sigma_{cyt}(\omega)\right)r_{ext}{}^3 + \left(\sigma_{mem}(\omega) - \sigma_{cyt}(\omega)\right)r_{int}{}^3} \tag{37}$$

with

$$\sigma_{mem}(\omega) = \sigma_{mem} + j\omega\varepsilon_{r,mem}\varepsilon_0 \tag{38}$$

$$\sigma_{cyt}(\omega) = \sigma_{cyt} + j\omega\varepsilon_{r,cyt}\varepsilon_0 \tag{39}$$

$$\sigma_{elec}(\omega) = \sigma_{elec} + j\omega\varepsilon_{r,elec}\varepsilon_0 \tag{40}$$

σ_{elec}, σ_{cyt}, and σ_{mem} are the electrical conductivity of the electrolyte, the cytoplasm, and the membrane, respectively. $\varepsilon_{r,elec}$, $\varepsilon_{r,cyt}$, and $\varepsilon_{r,mem}$ are their relative electrical permittivities, respectively. r_{int} and r_{ext} represent the inner and outer radius of the cell, respectively. ρ_v is the volume ratio of cells in the sample.

4.2 Sample Preparation and Characterization

Yeast cell samples were obtained by dissolving dry cells in water with ratio of 1:6 to obtain a volume ratio of approximately $\rho_V = 0.5$ (hydrated yeast cells have a water percentage around 66%). Deionized water and calibrated solutions are commercial products, which do not need specific preparation.

The intrinsic properties of all samples and their complex conductivity were computed using models presented in the previous section "Samples choice and modeling." The yeast cells sample was modeled using $\boldsymbol{\rho_V = 0.5}$, $\boldsymbol{\sigma_{cyt} = \sigma_{elec}} = 0.3$ S/m [23], $\boldsymbol{\varepsilon_{r,cyt} = \varepsilon_{r,elec}} = 78$, $\boldsymbol{\sigma_{mem}} = 0$ S/m and $\boldsymbol{\varepsilon_{r,mem}} = 5$ (lipid relative permittivity). Calibrated solutions were modeled using Eq. (40) with conductivity ($\boldsymbol{\sigma_{elec}}$) given by the manufacturer and the relative permittivity of water ($\varepsilon_{r,water} = 78$ at 25 °C). As the conductivity of deionized water is unknown, only its relative permittivity was modeled by setting the permittivity of pure water.

To verify the validity of our models, samples were characterized using high precision Liquid Test Fixture **16452A** (Keysight Technologies). Samples complex conductivity was extracted from impedance measurements using the manufacturer's formula. Both results for modeled and measured conductivities are shown in Figs. 15 and 16, which represent the apparent conductivity and apparent relative permittivity extracted for real and imaginary parts of complex conductivity using Eqs. (41) and (42), respectively.

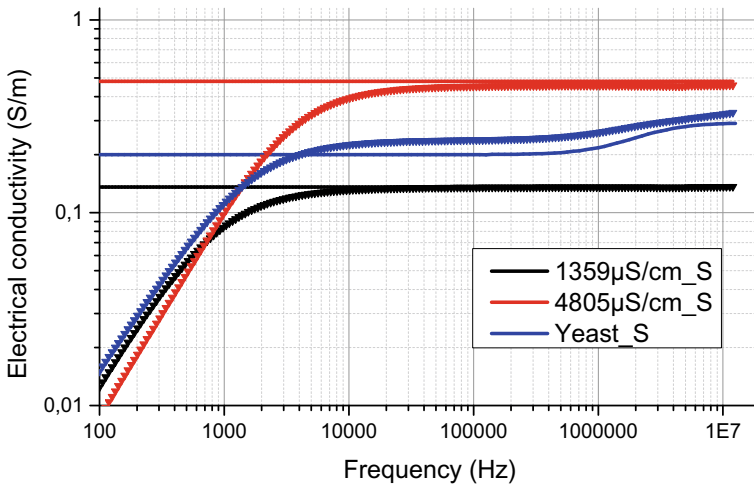$$\sigma_{app}(\omega) = \Re\big(\sigma_{samp}(\omega)\big) \tag{41}$$

Fig. 15 Apparent conductivity of the calibrated solution and yeast cells sample. Analytical simulation results (lines) and measurements (triangles)
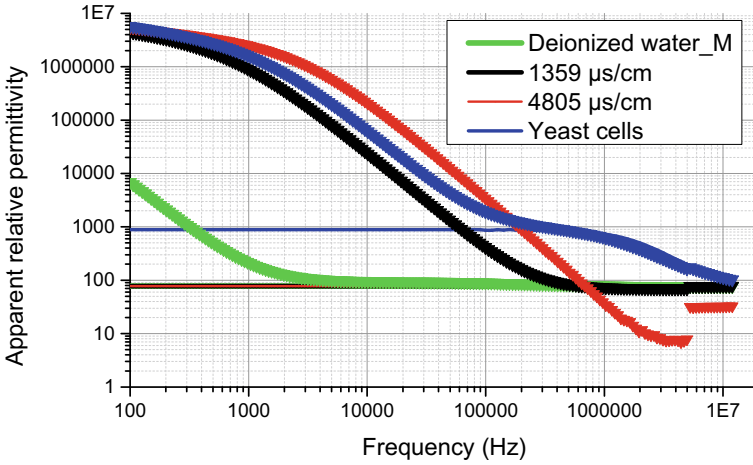
Fig. 16 Apparent relative permittivity of calibrated solutions and yeast cells sample. Analytical results (lines) and measurements (triangles)

$$\varepsilon_{r,app}(\omega) = \Im\left(\frac{\sigma_{samp}(\omega)}{\omega\varepsilon_0}\right) \tag{42}$$

One can see that the analytical model results are in concordance with measurements for upper frequencies, particularly for the cutoff frequencies of β dispersion. As mentioned before, this value is vital for the sensor design. It is necessary for the sensor to have a sufficient bandwidth around the β dispersion to correctly characterize a biological sample. The effect of the double layer, present only in measurement results, occurs at low frequencies and is not included in our analytical models. This choice is motivated because it is not an intrinsic property of the sample and depends mainly on electrode material and surfaces. One can see that this effect is quite the same for the yeast cells and calibrated solutions for both the conductivity and the relative permittivity. For deionized water, this effect occurs at very low frequencies and cannot be compared with other samples. At higher frequencies, the relative permittivity of all samples, except for the calibration solution with highest conductivity (500 μS/m), tends to 78 (permittivity of pure water). For the calibration solution with the highest conductivity, the high conductivity makes it difficult to extract the dielectric effect. Finally, for yeast cells, the second plateau is due to the cells membranes capacitances and is for this reason not present in the other measurements.

Results for measured conductivity and relative permittivity for all samples are synthesized in Table 4. The permittivity induced by double-layer effects is not presented, as explained above. The lower values for calibrated solutions can be explained by the lower temperature (conductivity is given for 25 °C). This table will serve as a reference for comparison with measurements made with the sensors (see next sections). The high value of apparent permittivity for the first plateau of yeast cells is induced by the high surface capacitance of cell membranes.

Table 4 Geometrical parameters for sensors C1 and C2

Sample	Conductivity (S/m)		Relative permittivity	
	1st plateau	2nd plateau	1st plateau	2nd plateau
Deionized water	0.001	NP*	78	NP[a]
1413 µS/cm solution	0,136	NP*	78	NP[a]
5000 µS/cm solution	0.455	NP*	~~32~~	NP[a]
Yeast cells	0.238	0.323	860	78

[a]*NP* not present

4.3 Sensor Fabrication

In this section, the impact of geometrical parameters was studied, such as the validity of our proposed methodology. For this, five sensor designs, named **C₁** to **C₅**, were fabricated. To be comparable, all sensors have the same sensing surface (1 mm × 1 mm). In this case, **L** is set to 1 mm for all sensors. For sensors **C₃** to **C₅**, the smallest electrode dimension (**w** or **g** parameters) was set to 5 µm. This represents the classical size of a yeast cell and corresponds to the most usual choice for sensor design. Setting the electrode dimension to the same order of size as the studied cells theoretically permits optimization of detection sensitivity: only one cell layer is enough to significantly modify the electric field between electrodes (setting of penetration depth). It is not useful to use smaller sizes because the investigated depth could be smaller than the cell sizes. Other parameters are set to obtain three different metalization ratios (0.2, 0.62, and 0.8) to study their impact. The C₁ sensor was designed using our proposed methodology. To obtain a sufficient bandwidth for the yeast cell model (approximately one decade before β dispersion), it was necessary to increase the initial cell gap of 5 µm to 20 µm with a metalization ratio of 0.6. The C₂ sensor was proposed to have an intermediate design between C₁ and C₃.

The sensors' parameters are shown in Table 5.

Sensors were fabricated using biocompatible materials, such as platinum, for electrodes and glass for the substrate. These choices and more details about fabrication were already discussed and presented in previous papers [10, 11]. Images of the five fabricated sensors are shown in Fig. 17.

Table 5 Geometrical parameters for sensors C₁ to C₅

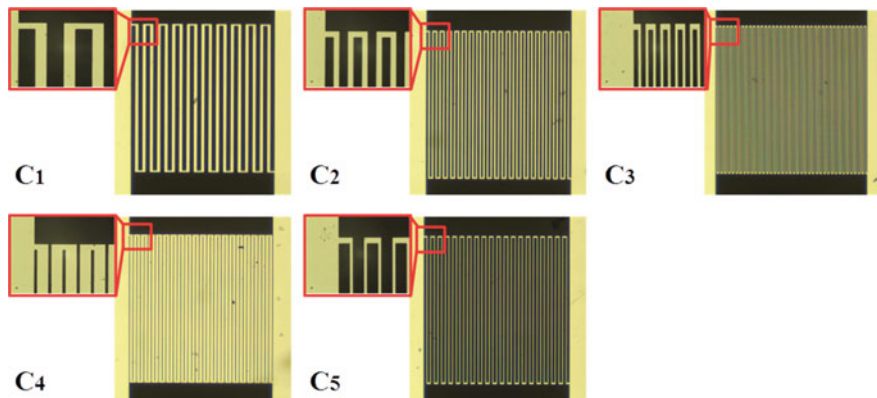| Sensor number	N (µm)	w (µm)	g (µm)	L (µm)	λ (µm)	η	Calculated K_{cell} (m⁻¹)
C₁	20	30	20	1000	100	0.6	90
C₂	40	15	10	1000	50	0.6	43
C₃	80	8	5	1000	26	0.62	21
C₄	40	5	20	1000	50	0.2	87
C₅	40	20	5	1000	50	0.8	30

Fig. 17 Optical microscope images of sensors C_1 to C_5 (magnifications $40 \times$ and 400x)

4.4 Sensor Characterization

All measurements with sensors were performed for a 2 µL volume of the sample deposited on the sensor surface using a micropipette.

The first characterization steps consist of the determination of the sensor cell factor $\mathbf{K_{cell}}$, which allows for deducing the sample conductivity from its impedance.

The characterization of an impedance-based sensor is typically divided according to the four following steps:

1. Measurement without a sample (unloaded measurement) to determine all capacitive effects of the measurement setup. In our case, capacitance is mainly due to the substrate and air electrical permittivity.
2. Short-circuit measurement to determine the impedances in series with sensors (if possible). This step is unnecessary if the impedance is not too low in comparison to cable and track impedances. This is the case for our sensors.
3. Measurement with calibrated solutions or well-known samples to determine the $\mathbf{K_{cell}}$ factor.
4. Determine the effect of the substrate. Knowing $\mathbf{K_{cell}}$ and the permittivity of air, it is possible to calculate the substrate permittivity.

Results for measurement without samples allows for extracting the apparent capacitance $\mathbf{C_{app}}$ from admittance, using Eq. (43). Capacitance was extracted at $\mathbf{f_0} = 1$ MHz because measurements are unstable at very low frequencies due to the high impedance induced. This corresponds to the central frequency in the bandwidth of interest. We obtain 1.02 nF, 1.69 nF, 3.28 nF, 1.11 nF, and 2.1 nF for the sensors C_1 to C_5, respectively.

$$C_{app}(\omega_0) = \frac{\Im(\sigma(f_0))}{2\pi f_0} \tag{43}$$

Results for measurements with calibrated solutions are displayed in Fig. 18. One can see first that all sensors except C_4 show a similar spectrum at low frequencies. This part of the spectrum is due to the double-layer effect and depends theoretically on the contact surface of the electrodes with the sample. Since sensors C_1, C_2, C_3 and C_5 present a close metalization ratio η (0.6−0.8), their surfaces in contact with sample are quite similar. C_4 shows a very small (0.2) ratio η compared to other sensors, and the effect on the impedance of the double layer is clearly higher than for the other sensors. This is particularly obvious when comparing it to C_1, which has close to the same cell factor as C_4. This result confirms our assumptions about the contribution of the parameter η. The increase of this parameter permits reduction of the effect of double-layer capacitance and increases the useful bandwidth.

Another important parameter is the electrode periodicity λ. We discussed the role of decreasing λ in the theoretical section that allows it to decrease penetration depth. Also, we assumed in the methodology section that increasing the electrode periodicity λ can increase the bandwidth of interest. The sensors C_1, C_2, and C_3 present similar factor η but three different lambda parameters: 100, 50, and 26, respectively. The
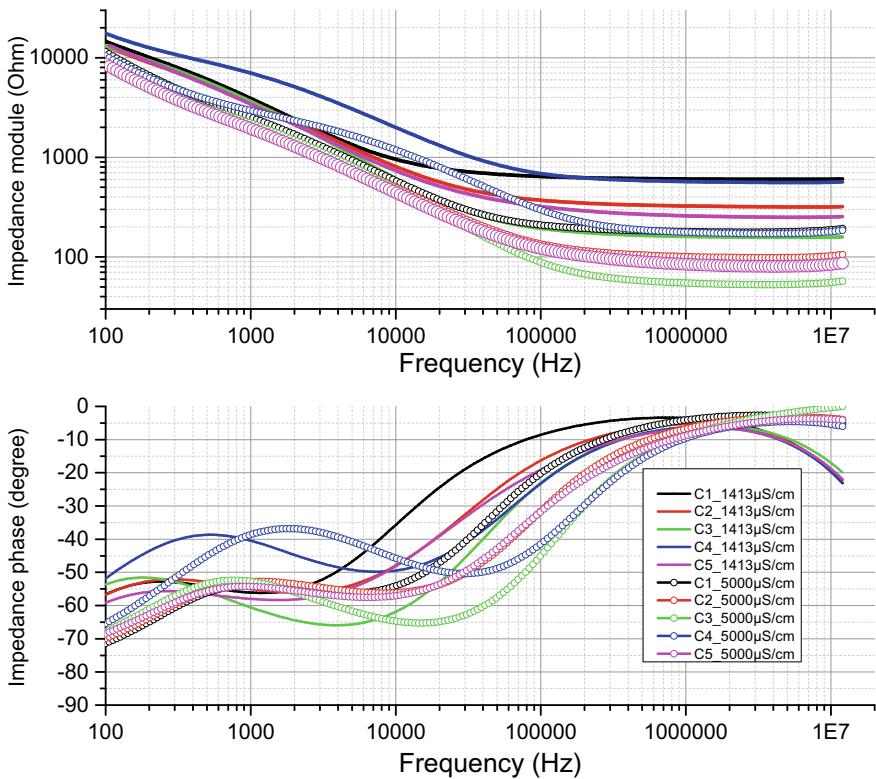

Fig. 18 Impedance in module and phase for sensors C_1 to C_5 for 1413 μS/cm and 5000 μS/cm calibrated solutions

Table 6 Measured and calculated K_{cell} for sensors C_1 to C_5

Sensor number	K_{cell} 1413 µS/cm	K_{cell} 5000 µS/cm	K_{cell} average	K_{cell} analytical	Error %
C_1	82.35	81.15	81.75	90	9.167
C_2	44.2	44.76	44.48	43	3.44
C_3	21.87	24.00	22.935	21	9.21
C_4	77.83	78.28	78.055	87	10.28
C_5	35.2	36.73	35.965	30	19.88

effects of these parameters are clearly visible in Fig. 18 results, mainly through the phase diagram. C4 shows a low cutoff frequency approximately twice lower than C_5, which also presents the same shift with C_6 for the same calibrated solutions. As we fixed the same surfaces for all sensors, it is unnecessary to discuss the effect of the electrodes' number for the same couple (λ, η). Nevertheless, we postulated in the theoretical section that the cell content of one pair of electrodes only depends on η. Following this, one can consider that sensors C_1, C_2, and C_3 have the same cell constant and the number of electrodes can be compared. C_3 has twice as many electrodes as C_2, as does C_2 compared to C_1. We clearly observe that the impedance module of the plateau decreases by a factor 2 from C_1 and C_2, and by a factor 2 from C_2 to C_3, as predicted.

These measurements also allow for determining K_{cell} for each sensor using Eq. (44). σ_{elec} and $\sigma(\omega)$ are the intrinsic conductivity and the complex conductivity of the electrolyte, respectively. f_0 is set to 1 MHz for the electrolyte at 1413 µS/cm and 3.3 MHz for the electrolyte at 5000 µS/cm. The results are synthesized in Table 6.

$$k_{cell} = \frac{\sigma_{elec}}{\sigma(f_0)} \tag{44}$$

These results are in concordance with the theoretical approach. The differences between the analytical model and the measures can mainly be explained by fabrication tolerances and some assumed simplifications in the analytical model (considering the semi-infinite layer) as well as the role of temperature (a variation of 1 °C implies approximately a 2% shift in electrolyte conductivity). The determination of K_{cell} permits calculation of the conductivity and permittivity of the samples. The permittivity of the substrate needs to be subtracted from the global measured results and can be calculated using Eq. (45) from the air measurement (Table 7).

$$C_{unload} = \frac{\varepsilon_O(\varepsilon_{r,sub} + \varepsilon_{r,air})}{K_{cell}} \Leftrightarrow \varepsilon_{r,sub} = \frac{C_{unload} K_{cell}}{\varepsilon_O} - \varepsilon_{r,air} \tag{45}$$

Final measurements were performed with biological samples (yeast cells) using the same protocol as the previous measurement. Results are given in Fig. 19 as a Bode diagram of the impedance. Only C_1 displays two distinct "plateaus," and it allows for measuring electrical properties of the biological sample before and after

Table 7 Measured relative permittivity of substrate for sensors C_1 to C_5

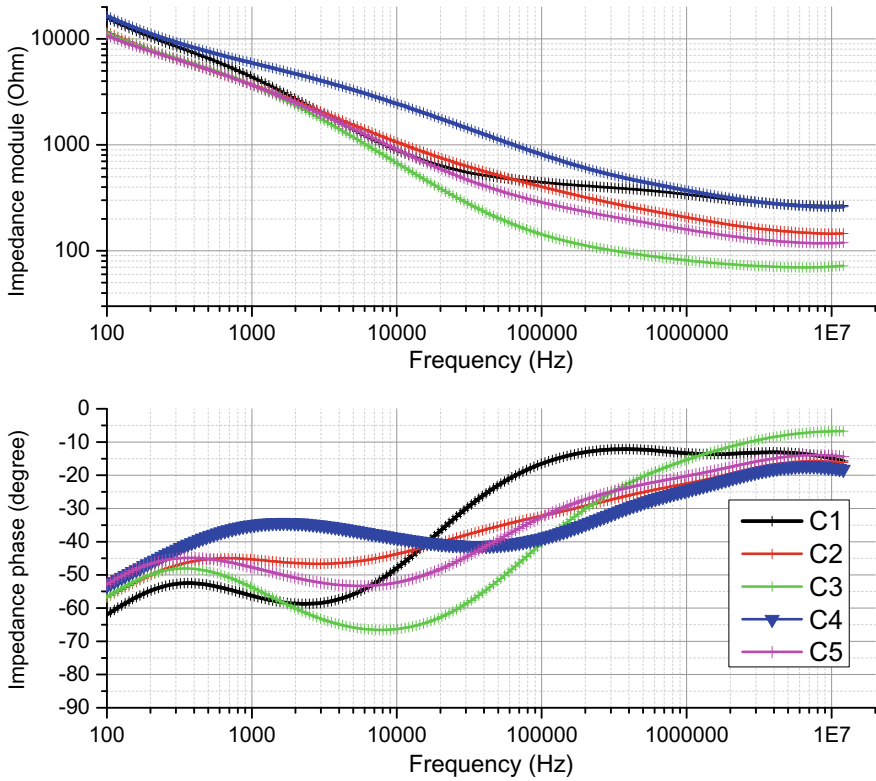| Sensor	C_{unload}	Calculated ε_{sub}
C_1	1.02E−12	8.42
C_2	1.69E−12	7.49
C_3	3.2E−12	7.29
C_4	1.11E−12	8.79
C_5	2.1E−12	7.53

Fig. 19 Impedance in module and phase for yeast cells sample measurement using sensors C_1 to C_5

β dispersion. This is clearly visible in the phase diagram by the presence of two lobes (local maxima) on each side of the β dispersion zone. Other sensors are not correctly optimized, and the double-layer effect occults the first part of the impedance response. This is especially visible by comparing C_1 and C_4, which have similar K_{cell} but not to the same degree of optimization. Their impedance diagrams are similar at higher frequencies, after β dispersion, but the first plateau is not visible for sensor C_4. Finally, intrinsic conductivity and permittivity of yeast cells sample were
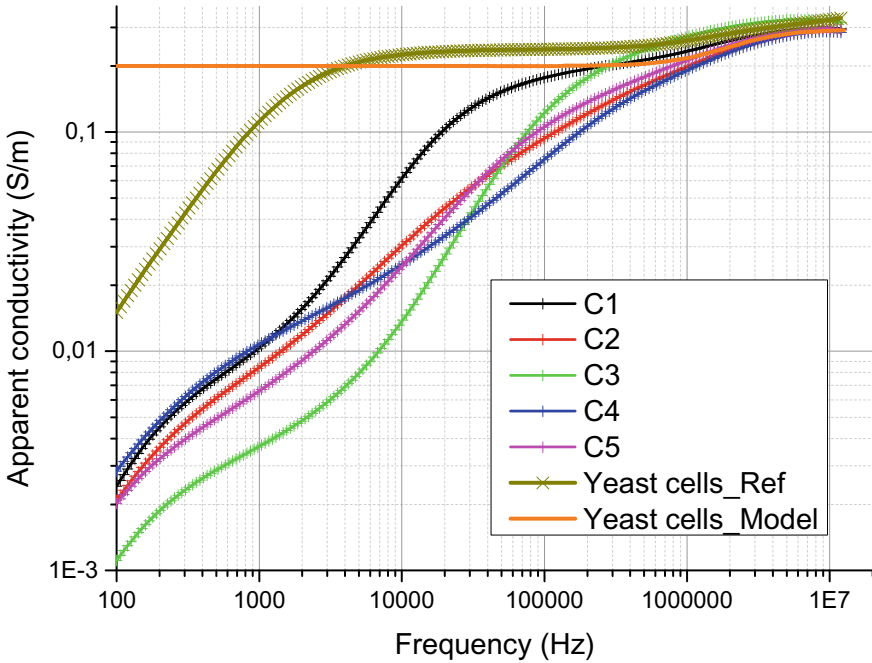
Fig. 20 Conductivity (real part of complex conductivity) of yeast cell samples calculated with the analytical model and extracted from measurement with liquid probe and sensors C_1 to C_5

extracted for impedance measurement using $\mathbf{K_{cell}}$ and presented in Fig. 20. These results are in concordance with theory and reference measurement and prove again that sensors others than $\mathbf{C_1}$ are unable to characterize yeast cells samples. The higher gap between $\mathbf{C_1}$ and the liquid text future results can be explained by the fast settling of yeast cells. The time necessary between sample deposition and measurement (1–2 min) is sufficient to obtain a greater cell concentration on the electrodes' surfaces. In terms of optimization, $\mathbf{C_1}$ represents the best compromise between penetration depth and the frequency band of interest for the targeted application, as proposed in the "optimization methodology" section.

5   Conclusion

A complete model for an interdigitated sensor was proposed and validated using FEM simulations. Using this model, the effect of all geometrical parameters on global impedance was studied to propose an optimization methodology. Electrodes with number $\mathbf{N}$ and length $\mathbf{L}$ permit adjusting impedance values to be compatible, for example, in the range of a measurement device without influencing the bandwidth.

The width and gap of the electrodes mainly influence penetration depth and bandwidth. Electrodes periodicity λ and metalization ratio η, depending only on **w** and **g** are more suitable to study the impact of **g** and **w**. An increase of η permits a reduction of the double-layer effect and simultaneously increases the useful bandwidth but must be limited to keep a correct uniformity on electric field distribution. A value of 0.6 appears to be the best compromise. The decrease of λ permits a reduction in the penetration depth for surface analysis but simultaneously decreases useful bandwidth. It may be adjusted to obtain the best compromise between the desired penetration depth and sufficient bandwidth. Measurements performed with five different sensors with the same active surface 1 mm × 1 mm, but different electrodes geometries were performed to validate our model and optimization methodology. The results obtained proved the necessity of optimizing interdigitated sensors using models and is a function of targeted applications. Sensors without sufficient optimization were unable to correctly characterize the biosample and extract its complex conductivity because the double-layer effect was too predominant. Sensor C_1, with the best optimization, was able to extract all useful parts of the complex conductivity.

Funding

References

1. L.C. Clark Jr., Monitor and control of blood and tissue oxygen tensions. Trans. Am. Soc. Artif. Intern. Organs. **2**(1), 41–48 (1956)
2. J.D. Newman (1997) Chemical sensor analysis, in *IEE Colloquium on Materials Characterization—How Can We Do It? What Can It Tell Us?* (Ref No 1997/150), pp. 6/1–6/3
3. E. Katz, I. Willner, Probing biomolecular interactions at conductive and semiconductive surfaces by impedance spectroscopy: routes to impedimetric immunosensors, DNA-sensors, and enzyme biosensors. Electroanalysis **15**(11), 913–947 (2003)
4. C. Gabriel, S. Gabriel, E. Corthout, The dielectric properties of biological tissues: I. Literature Survey. Phys. Med. Biol. **41**, 2231–2249 (1996)
5. P. Ertl, R. Heer Interdigitated impedance sensors for analysis of biological cells in microfluidic biochips. e & i Elektrotechnik und Informationstechnik**126**(1–2), 47–50 (2009)
6. J. Posseckardt, C. Schirmer, A. Kick, K. Rebatschek, T. Lamz, M. Mertig, Monitoring of *Saccharomyces cerevisiae* viability by non-Faradaic impedance spectroscopy using interdigitated screen-printed platinum electrodes. Sens. Actuat. B Chem. **255**, 3417–3424 (2018)
7. J. Wang, Electrochemical nucleic acid biosensors. Anal. Chim. Acta **469**(1), 63–71 (2002)
8. M. Ibrahim, J. Claudel, D. Kourtiche, M. Nadi, Geometric parameters optimization of planar interdigitated electrodes for bioimpedance spectroscopy. J. Electri. Bioimped. **4**(1), 13–22 (2013)
9. T.-T. Ngo, A. Bourjilat, J. Claudel, D. Kourtiche, M. Nadi, Design and realization of a planar interdigital microsensor for biological medium characterization, in: *Next Generation Sensors and Systems* (Springer, Cham, 2016), pp. 23–54

10. J. Claudel, A.L. Alves De Araujo, M. Nadi, D. Kourtiche, Lab-on-a-chip device for yeast cell characterization in low-conductivity media combining cytometry and bio-impedance. Sensors **19**(15), 3366 (2019)

11. A.L. Alves de Araujo, J. Claudel, D. Kourtiche, M. Nadi, Use of an insulation layer on the connection tracks of a biosensor with coplanar electrodes to increase the normalized impedance variation. Biosensors **9**(3), 108 (2019)

12. A.V. Mamishev, K. Sundara-Rajan, F. Yang, Y. Du, M. Zahn, Interdigital sensors and transducers. Proc. IEEE **92**(5), 808–845 (2004)

13. X. Hu, W. Yang, Planar capacitive sensors–designs and applications. Sensor Rev. (2010)

14. R. Igreja, C.J. Dias, Analytical evaluation of the interdigital electrodes capacitance for a multi-layered structure. Sens. Actuat. A Phys. **112**(2–3), 291–301 (2004)

15. R. Igreja, C.J. Dias, Extension to the analytical model of the interdigital electrodes capacitance for a multi-layered structure. Sens. Actuat. A Phys. **172**(2), 392–399 (2011)

16. D.C. Grahame, The electrical double layer and the theory of electrocapillarity. Chem. Rev. **41**(3), 441–501 (1947)

17. D.C. Grahame, Diffuse double layer theory for electrolytes of unsymmetrical valence types. J. Chem. Phys. **21**(6), 1054–1060 (1953)

18. K.B. Oldham, A Gouy–Chapman–Stern model of the double layer at a (metal)/(ionic liquid) interface. J. Electroanal. Chem. **613**(2), 131–138 (2008)

19. K. Bohinc, V. Kralj-Iglič, A. Iglič, Thickness of electrical double layer. Effect of ion size. Electrochim. Acta **46**(19), 3033–3040 (2001)

20. C. Gabriel, *Compilation of the Dielectric Properties of Body Tissues at RF and Microwave Frequencies.* King's Coll London (United Kingdom) Dept of Physics (1996)

21. O. Levy, D. Stroud, Maxwell Garnett theory for mixtures of anisotropic inclusions: application to conducting polymers. Phys. Rev. B **56**(13), 8035 (1997)

22. K.S. Cole, Electric impedance of suspensions of spheres. J. General Physiol. **12**(1), 29 (1928)

23. K. Asami, T. Hanai, N. Koizumi, Dielectric properties of yeast cells. J. Membrane Biol. **28**(1), 169–180 (1976)